J Mater Sci (2011) 46:1668–1679
DOI 10.1007/s10853-010-4984-4

Solid-state precipitation of stable and metastable layered compounds in thermoelectric $AgSbTe_2$

J. D. Sugar · D. L. Medlin

Received: 2 June 2010 / Accepted: 5 October 2010 / Published online: 28 October 2010

Abstract The precipitation of Sb_2Te_3 in Sb-rich $AgSbTe_2$ is studied by X-ray diffraction and electron microscopy. The results indicate that Sb_2Te_3 does not form directly, but rather through the precipitation of an intermediate metastable phase. Diffraction, energy-dispersive spectroscopy, and high-resolution transmission electron microscopy indicate that this intermediate phase has a nominal composition $(Ag,Sb)_3Te_4$ and a structure with a seven-layer stacking sequence rather than a five-layer one as in Sb_2Te_3. Two mechanisms based on experimental observations are proposed for the conversion of $(Sb,Ag)_3Te_4$ to Sb_2Te_3: evaporation–condensation and individual step motion. The microstructural evolution and mechanisms of the transformation are discussed in detail.

Introduction

Interfaces can enhance the properties of thermoelectric materials both through phonon scattering to reduce the thermal conductivity and by energy filtering to increase the Seebeck coefficient [1, 2]. These phenomena have motivated recent interest in developing nanostructured thermoelectric materials to take advantage of their high density of interfaces. One way to nanostructure bulk thermoelectric materials is to use controlled solid-state phase transformations to distribute nanoscale second phases [3–5]. This approach relies on knowledge of the microstructural evolution during a transformation so that nanoscale features can be tuned to the optimal morphology, number density, and composition. However, the compositional complexity of many high-performance thermoelectric systems, which can contain more than four components, complicates the phase diagram and ability to tune the microstructure over several length scales. Therefore, understanding the details of phase stability in these systems is necessary for the fabrication of bulk nanostructured materials.

Another challenge is that at the elevated temperatures required for thermoelectric power generation (~400 °C for $AgSbTe_2$), the embedded nanostructure must remain stable. Changes in precipitate morphology, volume fraction, and/or composition could have a deleterious effect on the thermoelectric properties. Therefore, in addition to understanding microstructural evolution for nanostructuring, it is also important to understand the mechanisms that control the long-term stability of multiphase thermoelectric systems.

In this study, we investigate the precipitation of tetradymite-structured Sb_2Te_3 within a rocksalt-structured Sb-rich $AgSbTe_2$ matrix. Compounds within the Ag–Sb–Te system are important in a number of thermoelectric systems, including Ag–Sb–Ge–Te [6] and Ag–Sb–Pb–Te [7]. While typically designated with 1:1:2 stoichiometry, the rocksalt-structured compound actually exists in a range of stable compositions between $Ag_{19}Sb_{29}Te_{52}$ and $Ag_{22}Sb_{28}Te_{50}$ [8–10]. For brevity, we refer to this compound as the δ phase.

The δ phase is known to have good thermoelectric properties with a thermoelectric figure of merit, *ZT*, as high as 1.3 at 427 °C [11–14]. One of the challenges with this material is that because of its complex phase equilibria, second-phase precipitates often form. When compositions of material are made outside the boundaries of δ stability, easily identifiable large-scale microstructural features can indicate two-phase material. For instance, material with the exact composition of $AgSbTe_2$ phase separates into a mixture of Ag_2Te precipitates in a δ matrix [9, 15].

J. D. Sugar (✉) · D. L. Medlin
Materials Physics Department, Sandia National Laboratories,
7011 East Ave., Livermore, CA 94550, USA
e-mail: jdsugar@sandia.gov

Alternatively, Sb_2Te_3 precipitates that are aligned along {111} planes in a typical Widmanstätten pattern form in Sb-rich material [16, 17]. The presence of Ag_2Te causes a characteristic sign change in the Hall coefficient [16, 17], which can be used to easily screen for single-phase δ material, but detection of Sb_2Te_3 requires microscopy or diffraction.

Here, we focus on the formation of Sb_2Te_3 precipitates in the δ phase at 500 °C. We show that Sb_2Te_3 formation does not proceed by a simple solid-state precipitation reaction, but through an intermediate step in which a metastable seven-layered structure forms. Our observation that an intermediate phase forms could aid in determining the exact composition boundaries of δ on the Sb-rich side of the pseudo-binary Ag_2Te–Sb_2Te_3 phase diagram.

In the subsequent text, we first provide background information on relevant layered chalcogenide structures in this system. Then, we show bulk X-ray diffraction data, electron diffraction data, compositional measurements, and atomic-scale images that demonstrate the presence of the seven-layered M_3Te_4 (M = Ag or Sb) structure as an intermediate phase in the formation of Sb_2Te_3. Finally, we discuss mechanisms for the formation of these intermediate phases and their relationship to the equilibrium Sb_2Te_3 precipitate phase.

Background on layered chalcogenide structures

In the thermoelectric chalcogenide systems, subtle changes in the metal (M)/chalcogen (Te) ratio can cause structural transformations. In rocksalt-structured tellurides, such as $AgSbTe_2$ and PbTe, the number of cations (M) and anions (Te) are approximately equal (M/Te $\approx$ 1). The removal of metal planes at regularly spaced intervals results in compounds with M/Te ratios less than unity. The five-layered, M_2Te_3 tetradymite structure is one example, but there are many others in the literature [18]. For example, in the Pb–Sb–Te system, PbTe and Sb_2Te_3 can form by the solid-state decomposition of the seven-layered compound "$Pb_2Sb_6Te_{11}$" [19–22]. It has also been shown that an excess of cations in Ge, Sn, or Pb-doped $(Bi,Sb)_2(Te,Se)_3$ leads to the formation of a continuous series of 1-D superstructures built up of sequences of five- and seven-layer lamellae [23, 24]. An important question is how to distinguish between these various structures? One method is by direct measurement of composition, which may be challenging for small differences in M/Te ratios. The following discussion of these layered crystal structures in the Ag–Sb–Te system provides information needed to detect compounds with intermediate composition between MTe and M_2Te_3 with electron diffraction.

In the rocksalt structure, the M/Te ratio is $\approx$1. In δ (i.e., $AgSbTe_2$), the cation sites (Ag and Sb) are disordered so that the probability of any cation site containing either Ag or Sb depends on the composition since the δ phase is stable over a range of compositions [8, 25, 26]. The structure of δ can be represented in terms of the stacking of the close-packed planes [23, 24]:

$$A\beta C\alpha B\gamma A\beta C\alpha B\gamma\cdots \tag{1}$$

where the capital Roman letters represent layers of Te atoms and the Greek letters represent layers of metal atoms (either Ag or Sb). Figure 1a shows the stacking as viewed along a $[\bar{1}10]$ crystallographic direction and the corresponding simulated electron diffraction pattern. The Te atoms are shown in green and the metal atoms are shown in red. In this relatively simple structure, the close-packed planes alternate between Sb/Ag and Te with no interruptions.

If the M/Te ratio is reduced to 0.667, the equilibrium precipitate phase, Sb_2Te_3, which has the tetradymite structure, forms. This structure is based on a rhombohedral unit cell, but it can also be described by its stacking sequence:

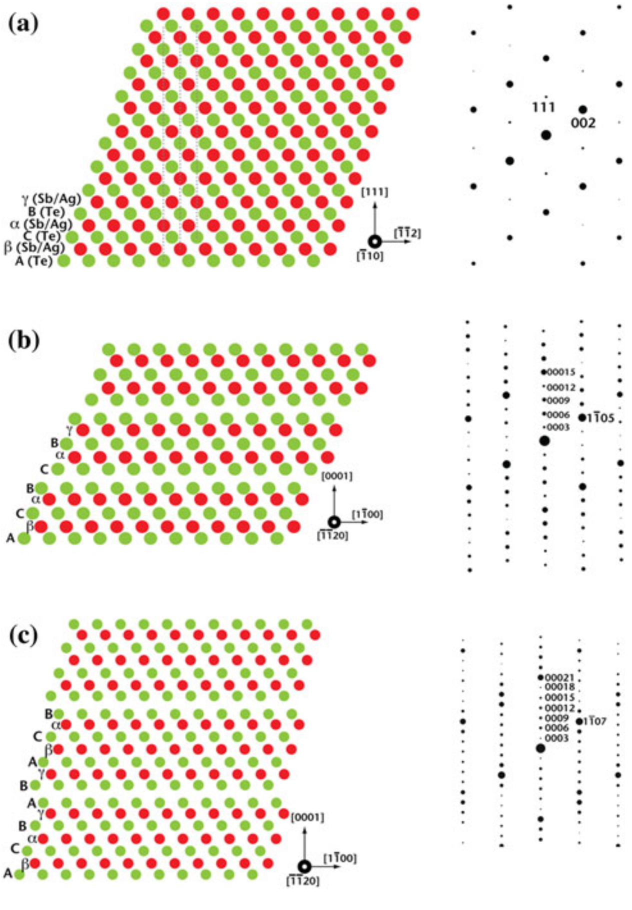

Fig. 1 Crystal structures and simulated electron diffraction patterns for (**a**) δ, (**b**) Sb_2Te_3, and (**c**) M_3Te_4 with the viewing directions indicated in each figure. In the simulated diffraction patterns, the five-layered Sb_2Te_3 structure and seven-layered M_3Te_4 structures are evident by the number of superlattice reflections between the fundamental reflections, 0 0 0 15 and 0 0 0 21, respectively

$$\underbrace{A\beta C\alpha B}_{5\text{ layers}}\ \underbrace{C\alpha B\gamma A}_{5\text{ layers}}\ \underbrace{B\gamma A\beta C}_{5\text{ layers}}A\cdots \qquad (2)$$

The tetradymite structure repeats sequences of five close-packed planes separated by a double-Te layer. A $[\bar{1}\bar{1}20]$ projection of this structure is shown in Fig. 1b. This structure results if one removes 1 plane of metal atoms every 6 planes from the rocksalt structure, and displaces the remaining 5-layered sections by $^{1}/_{3}[1\bar{1}00]$ to obtain the stacking sequence in (2). The five-layered stacking is also evident in the electron diffraction pattern because of the appearance of superlattice reflections at 1/5th the distance to the fundamental reflection, 0 0 0 15 (i.e., 0 0 0 3, 0 0 0 6, 0 0 0 9, and 0 0 0 12). A unit cell of Sb_2Te_3 contains 15 close-packed planes, or three 5-layer units.

Compounds with a metal/Te ratio between that of δ and Sb_2Te_3 can be formed by periodically removing a metal plane any n even number of close-packed planes with $n > 6$. For example, if a metal plane was removed every 8th close-packed plane ($n = 8$), a 7-layer structure would result (M_3Te_4). Similarly, the removal of every 10th close-packed plane ($n = 10$) results in a 9-layer structure (M_4Te_5). Additional compositional freedom is possible because compounds can be created that consist of linear combinations of several intermediate structures.

Figure 1c shows the results of removing every 8th close-packed plane and laterally shifting the remaining 7-layer units by $^{1}/_{3}[1\bar{1}00]$. The resulting M_3Te_4 structure can be described by the sequence of stacking in the close-packed planes:

$$\underbrace{A\beta C\alpha B\gamma A}_{7\text{ layers}}\ \underbrace{B\gamma A\beta C\alpha B}_{7\text{ layers}}\ \underbrace{C\alpha B\gamma A\beta C}_{7\text{ layers}}A\cdots \qquad (3)$$

The seven-layer stacking is evident in the simulated electron diffraction pattern because of the superlattice reflections at 1/7th the distance to the fundamental reflection, 0 0 0 21. Therefore, intermediate phases can be detected and distinguished from the equilibrium phases and each other by counting the number of superlattice reflections in the electron diffraction pattern. This information is used in the subsequent sections to interpret the diffraction and microscopy results.

Experimental procedures

Materials synthesis

To precipitate the Sb_2Te_3 compound in the solid state directly from δ, we chose a composition from the pseudobinary Ag_2Te–Sb_2Te_3 phase diagram [27] that would fall in the single-phase δ region at elevated temperature, but would become supersaturated in Sb_2Te_3 at reduced temperature. A 35 g ingot of material having an overall composition of 16.67 at.% Ag, 30.00 at.% Sb, and 53.33 at.% Te was fabricated from pure elements (99.999% pure Ag, 99.9999% pure Sb and Te, Alfa Aesar). The elements were sealed in a fused silica tube evacuated to a base pressure less than 5×10^{-7} torr. The sealed material was then melted in an upright tube furnace (Lindberg/Blue) at 850 °C for 3.5 h. The molten material was gently agitated three times during this period to promote mixing, and finally quenched in iced-brine solution.

Since the as-quenched microstructure is inhomogeneous and multiphase, the material was annealed to produce single-phase δ. Before performing this homogenization anneal, the material was extracted from the silica tube and the two ends were cut off with a low-speed saw (South Bay Technology, Inc., 660 Low-Speed Diamond Wheel Saw) equipped with a diamond blade (Allied High Tech Products, Inc.) to remove the majority of impurities that would have segregated to the ingot ends during solidification. Then, the remaining solidified material was resealed in an evacuated fused silica tube and annealed at 552 °C for 120 h.

The resulting single-phase material was cut into five pieces, which were then sealed in separate evacuated fused silica tubes. These samples were annealed at 500 °C for 5, 15, 30, 60, and 120 min to promote the formation of Sb_2Te_3 and then quenched into an iced-brine solution.

Materials characterization

Macroscopic structural information was obtained using an X-ray diffractometer (Scintag). Material was crushed in a mortar and pestle and scanned slowly at .03°/s from $2\theta = 20°–90°$ to avoid missing the diffraction peaks from any minor phases.

Electron diffraction and imaging were performed by transmission electron microscopy (TEM). Material was prepared for TEM using an abrasive slurry rotary disc cutter (South Bay Technology, Inc., 360 Rotary Disc Cutter) to cut 3 mm discs. These discs were thinned to electron transparency using mechanical dimpling (Gatan 656 Dimple Grinder) and liquid-nitrogen cooled ion milling (Gatan Dual Ion Mill and Fischione Instruments 1010 Ion Mill). Care was taken to ensure that the samples had cooled for at least 60 min before activating the ion beam to avoid damage and artifacts due to beam-induced heating. As a final step, the TEM samples were milled briefly with a low energy (1.5 kV) ion beam to clean the electron transparent regions.

Electron diffraction and high-resolution transmission electron microscopy (HRTEM) was performed on a JEOL 4000EX microscope operated at 400 kV with a LaB_6

emitter. Conventional imaging and diffraction, as well as compositional analysis, were performed on a JEOL 2010F (FEG) TEM operating at 200 kV and equipped with a SiLi EDS detector (Oxford Instruments). Electron diffraction and high-resolution phase-contrast TEM images were simulated using CrystalKitX and MacTempasX, respectively (Total Resolution LLC).

Quantitative analysis of EDS spectra was done using a Cliff–Lorimer ratio technique [28, 29]. The TEM EDS detector was calibrated with reference samples ($Ag_{16.7}Sb_{30.2}Te_{53}$ and $Ag_{0.8}Sb_{39.6}Te_{59.6}$) whose composition was measured on a calibrated electron microprobe analyzer (EMPA, JEOL JXA-8200). High-quality point EDS spectra from the δ and Sb_2Te_3 phases were recorded, but spectra from precipitates tens of nanometers wide (at intermediate time scales) could not be obtained because (1) sample drift prevented good counting statistics from point scans of a single precipitate, and (2) the matrix and precipitate compositions were similar and were difficult to deconvolute. Instead, we used multivariate statistical analysis (MSA) techniques on STEM-EDS spectrum images to quantify the finer-scale precipitate compositions. This approach provided an opportunity to correct sample drift by applying a cross-correlation correction at regular pixel intervals, and it provided statistics from thousands of spectra on which compositional measurements could be based. The EDS spectrum images were collected using drift correction at a size of 120 × 130 pixels, and with a 500 ms dwell time at each pixel. The spatially orthogonal [30] pure components corresponding to the phases present in the data matrix could then be found using multivariate statistical analysis (MSA) techniques with the Sandia-developed Automated eXpert Spectrum Image Analyzer software package (AXSIA [31, 32]). AXSIA can simplify the data matrix containing thousands of EDS spectra into a dimensionally reduced, physically relevant, and unbiased solution using MSA techniques such as principal component analysis (PCA), singular value decomposition (SVD), or multivariate curve resolution (MCR), the details of which can be found elsewhere [30, 33–36]. Once representative spectral shapes were obtained from the various small-scale precipitate phases, the compositions were determined. For this analysis, the peak intensities were quantified using a Nelder–Meade simplex method with the freely available spectrum analyzer software package from NIST, DTSA 2.5 [37].

Results

In the following experimental results, we first show that the evolution of second-phase precipitates proceeds with the formation of a metastable phase at intermediate anneal times. Then, we determine the structure and composition of this metastable phase through detailed electron microscopy observations. Finally, we consider the very early stages of the precipitation reaction and identify the presence of stacking faults due to the formation of double-Te layers. These results suggest mechanisms for the phase transformation, which we explore further in the "Discussion" section.

The evolution of second-phase precipitates

X-ray diffraction measurements revealed the expected equilibrium phases at early and late anneal times, but an intermediate phase that was neither δ nor Sb_2Te_3 was detected at intermediate anneal times. After the homogenization anneal at 552 °C, the material was single-phase δ. Figure 2a shows the X-ray diffraction pattern for the homogeneous δ phase after the 552 °C anneal (black) and a pattern for material that was annealed for 120 min at 500 °C (gray). Every peak visible in the homogeneous material can be identified as belonging to the δ phase (marked with a ◆) except for the peak located at $2\theta = 40.2°$. None of the Sb_2Te_3 reflections were visible in the homogeneous sample. After annealing at 500 °C, the precipitation of Sb_2Te_3 can be identified by the appearance of additional peaks in the pattern (marked with a ★), which are indexed in Table 1. The peak located at 40.2° persists before and after annealing at 500 °C with no change in intensity, so it is likely caused by some relatively inert impurity phase.

The Sb_2Te_3 grows to large, micrometer-scale, lamellar precipitates that are visible optically at late anneal times. These precipitates form a Widmanstätten pattern similar to what is seen in the PbTe-Sb_2Te_3 system [20], and are often found in high density near grain boundaries. Micrographs of this can be found elsewhere [38, 39]. When early and late-stage samples are investigated with HRTEM, the double-Te layers in the tetradymite structure become easily visible as modulations in contrast. As an example of this, Fig. 2b and c show phase-contrast images and diffraction patterns of the δ phase and Sb_2Te_3 phase, respectively. Our HRTEM image simulations confirm that the regularly spaced bright fringes in (c) are aligned with the double-Te layers and correspond to the positions between the atomic columns. The bright fringes in (c) occur on every 5th close-packed plane, which is consistent with the periodicity expected for the Sb_2Te_3 tetradymite structure (e.g., Fig. 1b).

Inspection of the X-ray diffraction data at intermediate annealing times reveals peaks that do not belong to either Sb_2Te_3 or δ. Figure 3a shows a detailed view (37°–41°) of the background subtracted X-ray data at each time interval after annealing at 500 °C. A peak is visible at 39.2°, which does not correspond to the Sb_2Te_3 phase. As time increases, the intensity shifts from the peak at 39.2° to the peak at 38.3°, the location of the $1\,0\,\bar{1}\,10$ reflection in Sb_2Te_3. The counts for each peak were integrated and plotted as a function of time in Fig. 3b. The peak intensity variation in time shows

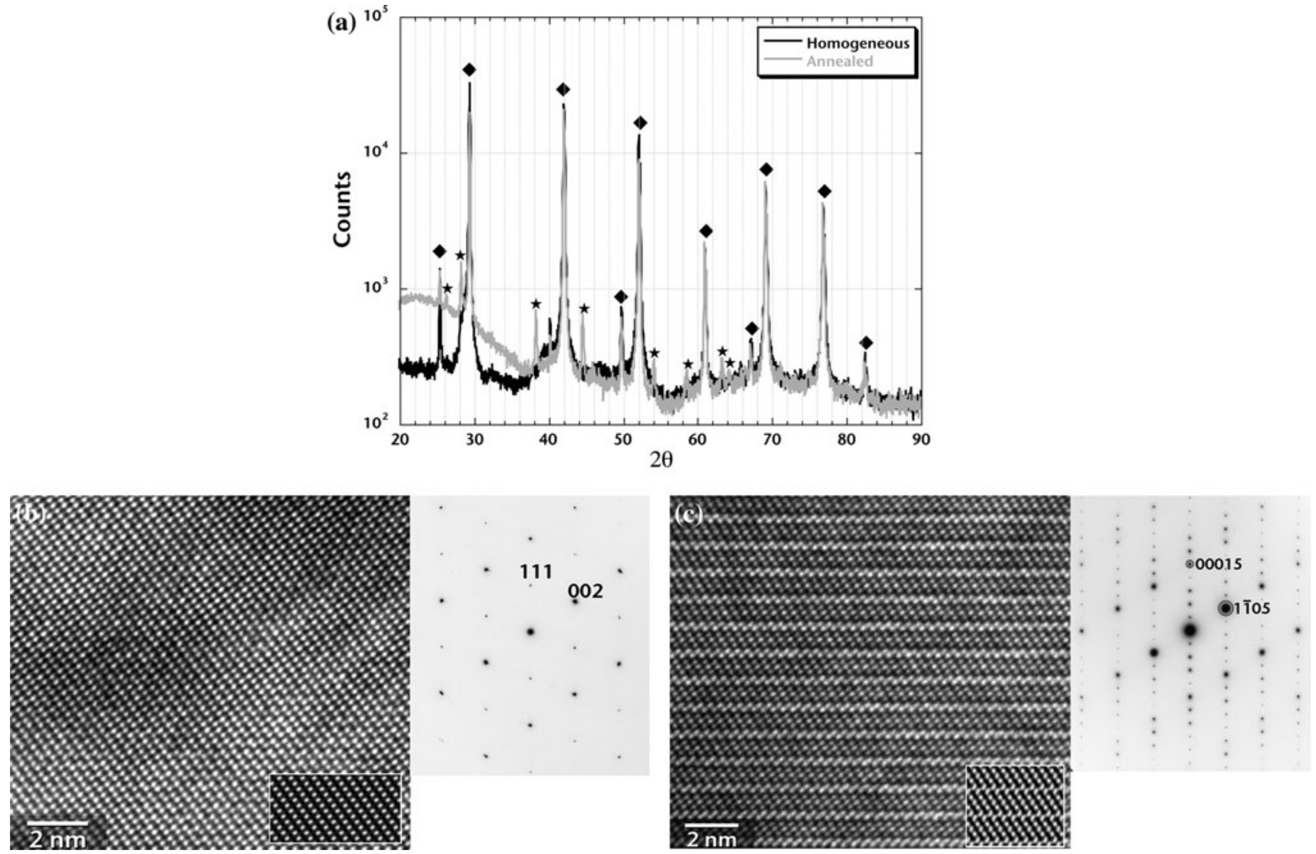

Fig. 2 (**a**) Powder X-ray diffraction data from "homogeneous" (552 °C, 120 h) and annealed samples (500 °C, 120 min). Peaks from the δ phase are marked with a *filled diamond* symbol while peaks from the Sb_2Te_3 phase are marked with a *filled star*. Peaks are indexed in Table 1. The Sb_2Te_3 peaks appear after the anneal at 552 °C. Corresponding HRTEM image and electron diffraction patterns of rocksalt δ (**b**) and Sb_2Te_3 (**c**) with inset simulated images (**b** defocus = −230 Å, thickness = 56 Å; **c** defocus = −230 Å, thickness = 40 Å). The bright contrast corresponds to regions between atomic columns. The positions between the double-Te and every 5 close-packed planes in (**c**) are evident by their bright contrast. The corresponding diffraction pattern shows superlattice reflections at 1/5th the distance to the fundamental 0 0 0 15 reflection

that the intensities of the peaks at 39.2° and 38.3° are inversely related. As the Sb_2Te_3 peak increases in intensity, the peak at 39.2° decreases in intensity. Although the data are not shown in the figure, a similar shift of intensity is also observed at lower angles. For instance, an extra peak at 28.5° forms at early times and then decays as the $1\ 0\ \bar{1}\ 5$ Sb_2Te_3 reflection intensifies at 28.3°.

These X-ray diffraction results suggest that an intermediate phase, which is responsible for the X-ray diffraction peak at 39.2°, forms before Sb_2Te_3 and is eventually consumed or replaced as the Sb_2Te_3 grows. To test this hypothesis, we investigated the structure and composition of the second phases at intermediate times using TEM.

Structural and compositional determination of the intermediate phase

Figure 4a–c show electron micrographs and electron diffraction patterns from a sample after it was annealed at 500 °C for 5 min. In the bright-field image in Fig. 4a, fine features that appear as long straight lines or lamellae can be seen that are ~10 nm wide. In the corresponding electron diffraction pattern, additional reflections appear that do not correspond to the cubic δ phase. These extra reflections are equally spaced at intervals of 1/7th the distance to the fundamental reflection, similar to the simulated diffraction pattern in Fig. 1c for the postulated M_3Te_4 structure.

Dark-field images and corresponding diffraction patterns confirm that the lamellae are associated with the **g**/7 superlattice reflections. In Fig. 4b, the sample was tilted to excite the 222 systematic row in the matrix phase. Since the superlattice reflections from the second phase are aligned with the close-packed {111} planes of the matrix, this condition excites the superlattice reflections. When an imaging condition of $\mathbf{g} = 0\,0\,0\,21_{M_3Te_4} \| 222_\delta$ (the fundamental 0 0 0 21 reflection that is parallel to the 222 reflection of the matrix) is used for dark-field imaging, only

Table 1 Indexed X-ray diffraction peaks for Fig. 2a

2θ (°)	*d*-spacing (Å) (measured/ theoretical)	*h*	*k*	*i*	*l*
δ					
25.44	3.50/3.51	1	1	–	1
29.44	3.03/3.04	2	0	–	0
42.04	2.15/2.15	2	2	–	0
49.92	1.82/1.83	3	1	–	1
52.21	1.75/1.76	2	2	–	2
61.08	1.52/1.52	4	0	–	0
67.24	1.39/1.39	3	3	–	1
69.10	1.36/1.36	4	2	–	0
76.83	1.24/1.24	4	2	–	2
82.41	1.17/1.17	5	1	–	1
Sb_2Te_3					
26.44	3.37/3.38	0	0	0	9
28.30	3.15/3.16	0	1	$\bar{1}$	5
38.32	2.35/2.35	1	0	$\bar{1}$	10
44.62	2.03/2.03	0	0	0	15
54.21	1.69/1.69	0	0	0	18
58.65	1.57/1.58	0	2	$\bar{2}$	10
63.52	1.46/1.47	1	0	$\bar{1}$	19
64.23	1.45/1.45	0	0	0	21

the lamellae perpendicular to **g** became bright.[1] Similarly, in Fig. 4c, the sample was tilted so that a $2\bar{2}2$ systematic row was excited and the dark-field imaging condition utilized $\mathbf{g} = 0\,0\,0\,21_{M_3Te_4} \| 2\bar{2}2_{\delta}$. In this case, the other orientation of lamellae appeared bright in the image. Again these lamellae are perpendicular to **g** and they are rotated 70.1° from the lamellae in Fig. 4b, which is consistent with the angle between the {222} and $\{2\bar{2}2\}$ planes (70.5°) in the cubic structure.

Although the electron diffraction data are consistent with the proposed seven-layered, M_3Te_4 structure in Fig. 1c, other possibilities should be considered for this intermediate phase. For example, the literature has suggested an alternative M_3Te_4 rucklidgeite structure based on a "555525555" stacking sequence (a "5" represents a M_2Te_3 unit and a "2" represents a double-M layer) [18], but this would have a diffraction pattern very different from the ones observed in Fig. 4. Another possibility is the M_4Te_3 pilsenite structure [18, 40], which has a similar diffraction pattern to M_3Te_4, but a structure based on "52" stacking and a slightly different stoichiometry. To resolve this ambiguity, we conducted HRTEM observations and measured the composition of the lamellae using EDS.

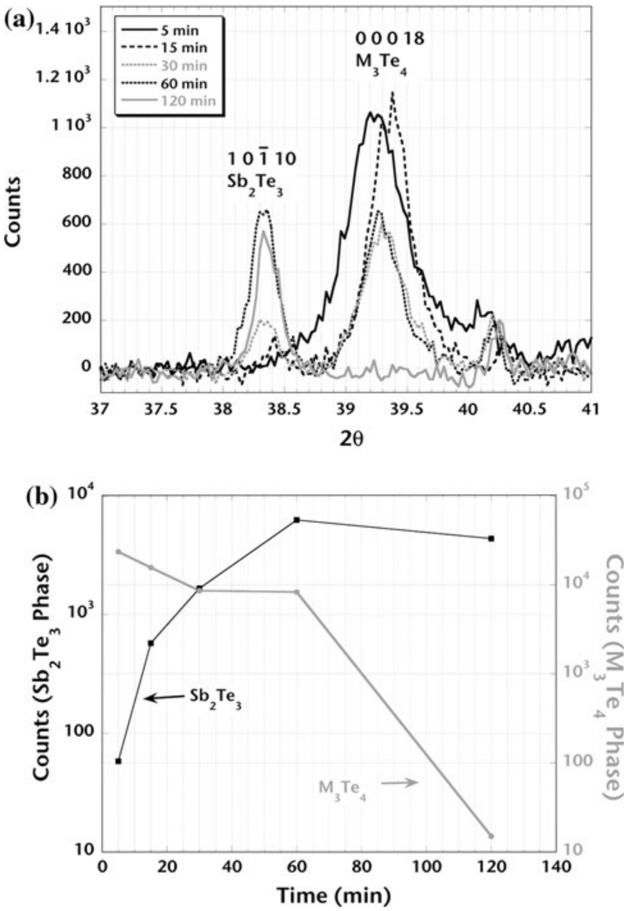

Fig. 3 (**a**) X-ray diffraction data for samples annealed for 5, 15, 30, 60, and 120 min at 500 °C at $2\theta = 37°–41°$. Extra diffraction peaks corresponding to the intermediate M_3Te_4 phase are visible. The integrated intensity of the peaks after background subtraction is shown in (**b**) as a function of time. The variation in peak intensity with time suggests that as Sb_2Te_3 forms, the metal-enriched intermediate phase, M_3Te_4, is consumed

The HRTEM image in Fig. 4d is from a region similar to the region from Fig. 4a–c, but shown at higher magnification. The corresponding electron diffraction pattern has reflections from both the matrix δ phase and the precipitate phase because the selected area aperture is too large to select only the tens of nm wide precipitates. In the image, it is possible to count the number of close-packed planes between the bright fringes (double-Te layers), which results in the expected 7-layer sequence. There is a small discrepancy in the distance between the double-Te layers in the image and simulation. The image simulation is not exact because this structure is estimated from the Te–Te and Te–Sb bond lengths in Sb_2Te_3. These bond distances would likely be different in the actual M_3Te_4 structure, causing the observed differences between the image and

---

[1] Since the objective aperture was too large to limit the illumination in the dark-field image to the 0 0 0 21 reflection only, both the 0 0 0 21 and 0 0 0 18 reflections were within the limits of the objective aperture.

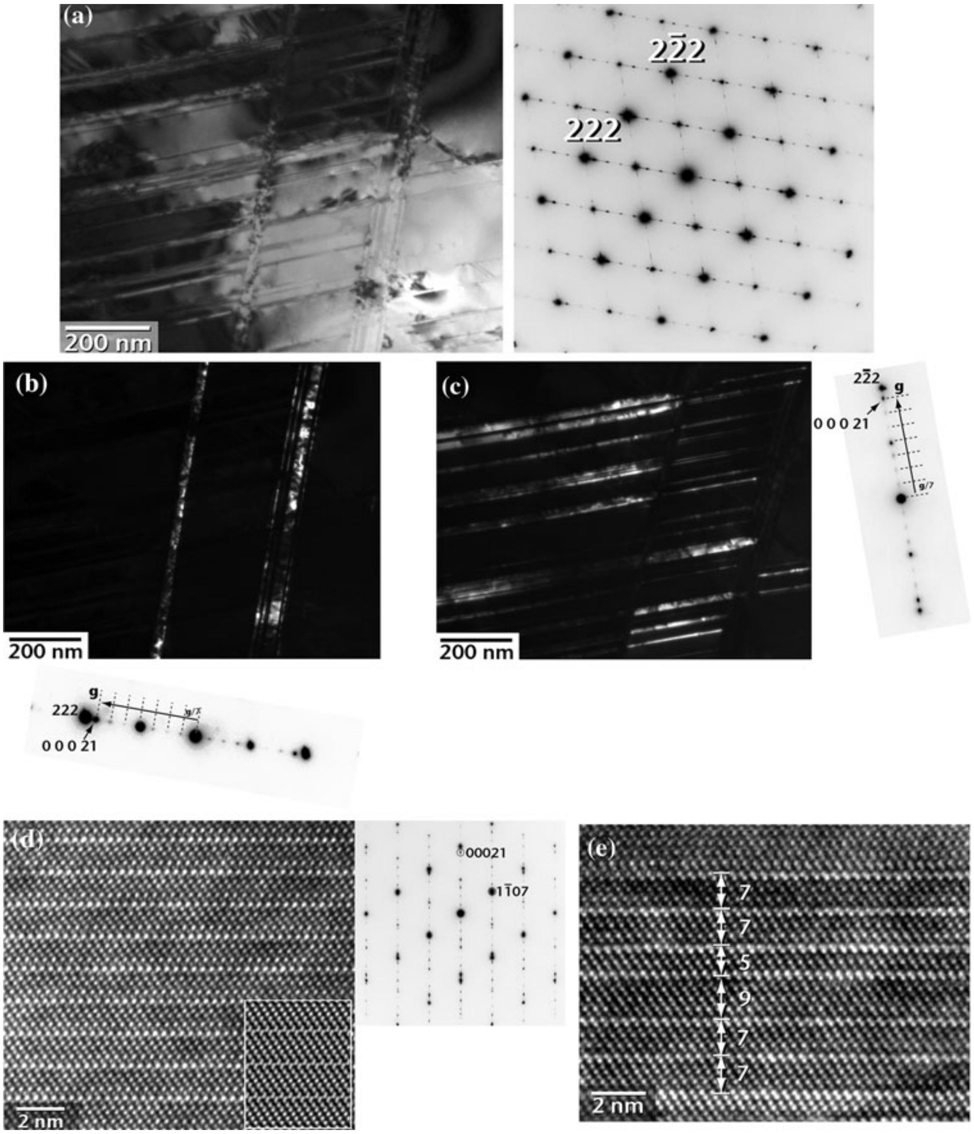

Fig. 4 (**a**) BF image and diffraction pattern of a sample annealed for 5 min at 500 °C. The diffraction pattern shows δ and additional superlattice reflections. The DF images formed with the 0 0 0 21 reflections in (**b**) and (**c**) show that thin precipitate plates $\approx$10 nm wide correspond to the extra superlattice reflections at **g**/7. The image and simulation in (**d**) (defocus = −180 Å, thickness = 60 Å) shows seven close-packed plane layers between double-Te layers. The electron diffraction pattern superposes the δ and M_3Te_4 patterns, and the superlattice reflections at 1/7th of 0 0 0 21 in Sb_3Te_4 are visible. The image in (**e**) shows a region of an intermediate stage precipitate at high magnification in which the double-Te layer ordering varies between five, seven, and nine-layer spacings

simulation. A structural refinement on the M_3Te_4 structure would help to more accurately simulate HRTEM images. In spite of these differences, the main observation is that the double-Te layers occur every seven close-packed planes and no double-M layers are observed. Neither the "555525555" Bi_3X_4 [18] nor the "52" M_4Te_3 [40] structures are consistent with the observed double-Te spacing.

Finally, we measured the composition of the lamellae with EDS in the TEM. Figure 5a shows a bright-field (BF) STEM image with lamellae from a sample annealed for 15 min at 500 °C. In the image, two orientation variants of the thin-plate precipitates are seen. The sample was tilted so that the precipitates were approximately edge on to avoid compositional variations through the sample thickness (but not directly edge on to avoid channeling effects), and the boxed region was selected for an EDS spectrum image. The results of a spatially orthogonal (abundance initializer) multivariate curve resolution (MCR) done with the AXSIA software package [30] is shown in the composite maps (inset) and corresponding spectra in Fig. 5a. The composite map shows the relative intensities and spatial distributions of the corresponding yellow and blue pure component spectra. Qualitatively, the spectra show that the plates are slightly enriched in Sb and Te and the matrix is slightly enriched in Ag. Because of the closeness of composition of the two phases, the maps are somewhat noisy. At any specific pixel location in the composite image, however, there is very little intensity mixing of the two pure components. This verifies that the composition is uniform through the sample thickness at this tilt condition, and that the pure component spectral shapes approximate the two phases present.

The composition of the elements in the precipitates at various stages in the precipitation reaction verifies an intermediate composition of M_3Te_4 at intermediate anneal times. We measured the composition of the precipitate and matrix phases at intermediate and late times in the precipitation reaction. We compared these results with the homogeneous δ phase at $t = 0$. The averaged results of the quantification are shown in Table 2 and plotted in Fig. 5b. The elemental compositions indicate that at intermediate times a compound with the approximate composition $Ag_{17.6}Sb_{27}Te_{55.4}$ (M/Te = 0.81) forms, which is approximately consistent with the postulated M_3Te_4 (M/Te = 0.75) compound. The deviations in the measurement from Sb_2Te_3 stoichiometry at late times could be associated with error or actual compositional deviations in the sample. There is likely some systematic error that results from potential offsets in the EMPA calibrations as well as from the deconvolution of the overlapping Sb and Te L X-ray peaks. In addition, defects such as vacancies or anti-site defects could cause detectable compositional deviations as previous measurements of vacancy concentration in δ were nominally 4%, but reached values as high as 13% [26].

In summary, the analytical data are all consistent with the formation of an intermediate phase, M_3Te_4. Now, it is possible to use this information to describe the matrix-precipitate orientation relationship and to explain the X-ray diffraction peak at 39.2° in Fig. 3a. The crystallographic alignment of the M_3Te_4 lamellae with the matrix phase is evident in the diffraction patterns in Fig. 4. With the proper indices corresponding to the M_3Te_4 structure of Fig. 1c identified on the diffraction patterns, we can specify the crystallographic orientation relationship between the precipitate and matrix phase as:

$$\{111\}\langle 1\bar{1}0\rangle_{\delta} \| \{0001\}\langle 11\bar{2}0\rangle_{M_3Te_4}, \tag{4}$$

which is equivalent to the orientation described for Sb_2Te_3 in δ and Sb_2Te_3 in rocksalt PbTe [22, 38]. Finally, based on the electron diffraction data of Fig. 4, the measured d-spacing of the 0 0 0 18 planes in the intermediate M_3Te_4 structure is 2.30 Å, which corresponds to an X-ray diffraction peak position of $2\theta = 39.1°$. Similarly, the extra peak at 28.5° (not shown in the figure) can be attributed to the 1 0 $\bar{1}$ 7 reflection in M_3Te_4.

Although the seven-layered structure is the most commonly observed intermediate phase throughout the

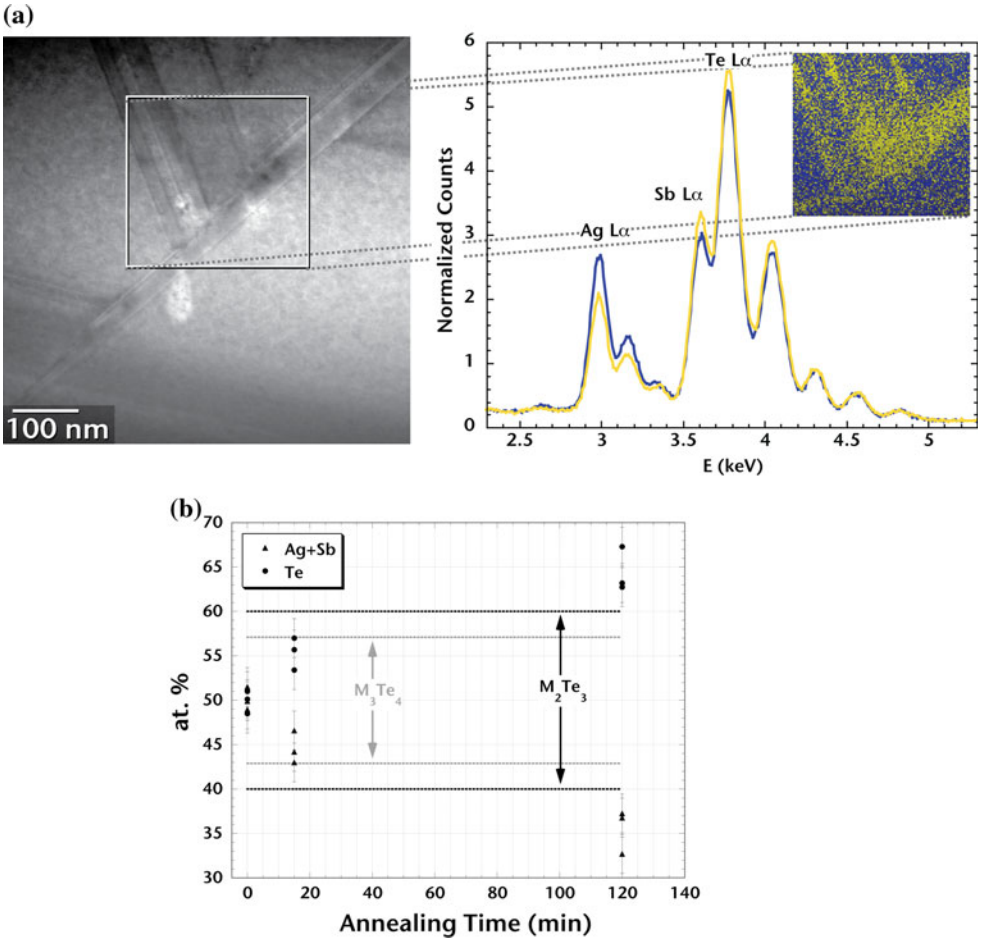

Fig. 5 (**a**) BF STEM image of a region of sample after the 15 min anneal and the *boxed region* identified where an EDS spectrum image was collected. The spatially orthogonal principal spectra and a composite map (*inset*) show that the precipitate plates are enriched in Sb and Te relative to the matrix phase as expected. The plot in (**b**) shows the results of a quantitative Cliff–Lorimer analysis of several precipitate spectra. As annealing time is increased the composition of the precipitates approximates Sb_2Te_3 and passes through the composition of M_3Te_4 at intermediate times

Table 2 Elemental concentrations of phases measured by EDS (Cliff–Lorimer)

Annealing Time (min)	Concentration in at.%		
	Ag	Sb	Te
0 (δ phase)	23.3 ± 1.5	26.8 ± 1.4	49.9 ± .7
15 (M_3Te_4)	17.6 ± 2.6	27.0 ± 2.1	55.4 ± 1.1
120 (M_2Te_3)	4.4 ± .8	31.2 ± 2.0	64.4 ± 1.5

precipitation reaction, in some cases we see variation in the spacing of the double-Te layers. This is evident in the HRTEM image shown in Fig. 4e. The bright fringes corresponding to the double-Te layers are observed at intervals of 5, 7, and 9 close-packed planes. This observation suggests that understanding the initial formation and subsequent rearrangement of double-Te layers may provide clues to the mechanisms of the transformation.

Early-stage formation of double-Te layers as stacking faults

To better understand the initial formation of the double-Te layers, we investigated the microstructure of the as-quenched material using TEM. Although, the bulk X-ray diffraction data (homogeneous in Fig. 2a) show that no other phases are present in a significant amount, the electron microscopy reveals many planar defects. As shown in Fig. 6a and b, these defects have the usual bright/dark fringe contrast commonly observed for stacking faults inclined relative to the viewing direction [29]. We also conducted systematic tilting experiments to establish the character of these faults. In Fig. 6b, the invisibility criterion is satisfied for the faults in (a) that run from the lower-left to the upper-right corner of the image. With the imaging condition, $\mathbf{g} = \bar{2}20$, identified in the image, the invisibility criterion suggests a displacement vector, $\mathbf{R} = \pm[hhl]$, to satisfy $\mathbf{g} \cdot \mathbf{R} = 0$. Images of the same area were recorded from 4 additional zone axes and 12 additional Bragg scattering conditions to uniquely determine $\mathbf{R}$ for these stacking faults. Additional invisibility conditions were found for $\mathbf{g} = 2\bar{4}2$ and $\mathbf{g} = 02\bar{2}$, which suggests that $\mathbf{R} = \pm h[111]$.

There are two possible types of stacking faults in this rocksalt compound that can produce a double-Te or double-metal layer. Consider an example in which a single metal layer is removed from the rocksalt structure. The resulting stacking fault would have $\mathbf{R} = {}^1\!/_6[\bar{1}\bar{1}\bar{1}]$, i.e., $A\beta C\alpha B\gamma A \xrightarrow{\text{remove } \alpha} A\beta CB\gamma A$. This type of translation, however, would cause a jog in the stacking between the C and B planes because of the missing A in the sequence. Another possibility is that after the metal layer is removed, half of the crystal is translated by ${}^1\!/_6[1\bar{2}1]$, i.e.,

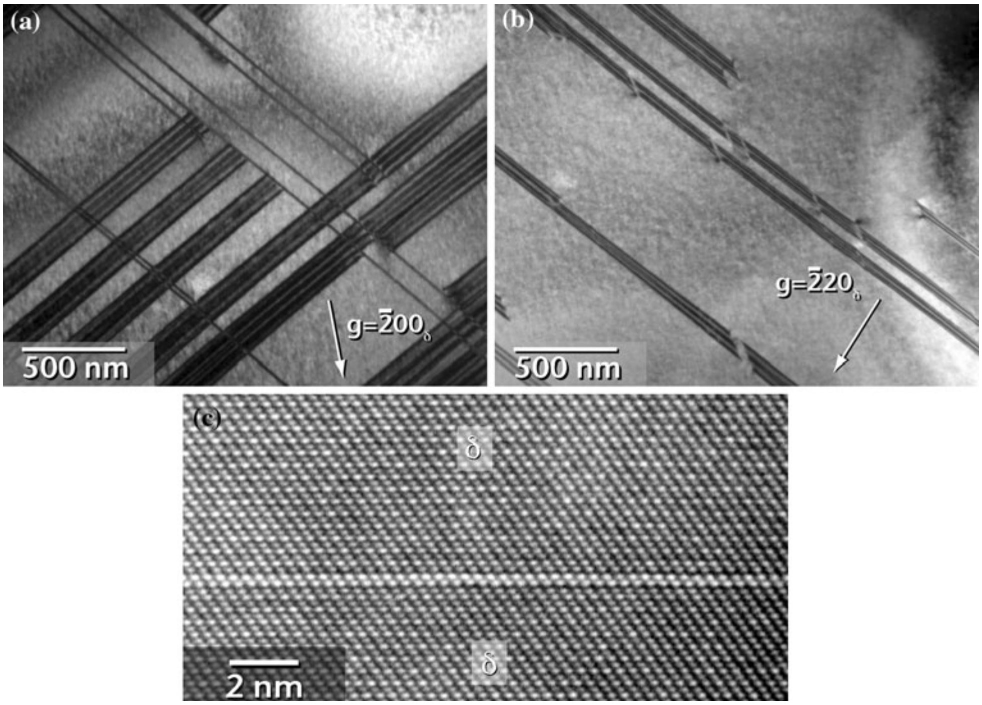

Fig. 6 Bright-field TEM images (**a**) and (**b**) of stacking faults in δ with $\mathbf{R} = {}^1\!/_6\langle\bar{1}\bar{1}\bar{1}\rangle$ recorded under different imaging conditions. The images are from the same region of the sample, and in (**b**) all of the faults that run from the *lower-left* to the *upper-right* corner of the image are invisible because the invisibility criterion $\mathbf{g} \cdot \mathbf{R} = 0$ is satisfied. In (**c**), a defect similar to the features in (**a**) and (**b**), but with $\mathbf{R} = {}^1\!/_2\langle 0\bar{1}0\rangle$ at high magnification shows a single bright fringe, consistent with simulations of a single double-Te layer

$A\beta CB\gamma A \overset{\text{translate } B\gamma A}{\longrightarrow} A\beta CA\beta C$, which leads to a total translation $\mathbf{R} = {}^{1}\!/_{6}[\bar{1}\bar{1}\bar{1}] + {}^{1}\!/_{6}[1\bar{2}1] = {}^{1}\!/_{2}[0\bar{1}0]$. This type of stacking fault does not have a jog in the stacking and exhibits little contrast for most low-index imaging conditions ($\mathbf{g} = 020$ or 220) because $\mathbf{g} \cdot \mathbf{R}$ is an integer. The faults in Fig. 6a and b have a displacement vector $\mathbf{R} = \pm h[111]$ and a habit plane of (111), determined from the electron diffraction patterns. These two fault geometries are consistent with either a double-Te or double-metal layer with a jog.

The HRTEM image in Fig. 6c is from a region containing a defect similar to the stacking faults shown in Fig. 6a and b. This image shows a single horizontal bright fringe near the middle of the image with no jog. The HRTEM image simulations suggest bright fringes correspond to the double-Te layers in the tetradymite structure as seen in Fig. 2c. Similar simulations confirm that a single double-Te layer would produce a single bright fringe like the one in Fig. 6c. Since this defect has no jog, it must have a translation vector $\mathbf{R} = {}^{1}\!/_{2}\langle 0\bar{1}0\rangle$, which is different than the defects shown in Fig. 6a and b and would be invisible ($\mathbf{g} \cdot \mathbf{R}$ = integer) for both of those imaging conditions. However, the HRTEM image confirms that stacking faults of double-Te do appear at early stages in the precipitation reaction. Therefore, we can postulate that the stacking faults in Fig. 6a and b are probably also due to individual double-Te layers and not double-M layers.

As noted above, the composition of the initially single-phase δ was selected to be $Ag_{16.7}Sb_{30}Te_{53.3}$, making the Te:M ratio slightly larger than 1. The formation of planar defects consisting of double-Te layers provides a way for the system to accommodate the excess Te. These faults can also serve as precursors to the intermediate phases. For this to occur, once the double-Te layers form, they must be able to rearrange themselves so that they can either (1) agglomerate to form a precipitate phase, or (2) move in some way to convert a metastable structure to the equilibrium five-layered structure. In the next section, we describe mechanisms that can explain this second-phase evolution.

Discussion

The preceding experimental observations suggest several stages in the precipitation of Sb_2Te_3 in δ. When the δ phase is initially quenched from the homogenization anneal, there is excess Te relative to the δ phase boundary. Initially, to accommodate this excess Te composition, isolated double-Te layers form in δ as shown in Fig. 6a, b, and c. As the precipitation reaction proceeds, the double-Te layers continue to precipitate from solution and eventually reach a high enough density in some regions to agglomerate at regularly spaced odd intervals of close-packed planes. This ordering produces intermediate compounds like the seven-layered M_3Te_4 phase, or the other structures like the one shown in Fig. 4e. In the final stages of the precipitation reaction, the double-Te layers eventually rearrange themselves into the five-layered Sb_2Te_3 sequence and form precipitates several microns wide. The transition compounds at intermediate stages in the reaction provide a transformation pathway of incremental structural changes as the two phases approach their equilibrium compositions.

How do the Te double layers rearrange to form these observed structures? In a previous article, we proposed a mechanism for the growth of existing tetradymite plates in rocksalt tellurides by the motion of interfacial steps [38]. The diffusive motion of these steps removes a metal plane from the rocksalt phase and forms a double-Te layer, thereby thickening the Sb_2Te_3 plate. The Te layers remain essentially fixed during the step motion, and the transformation occurs through a flux of metal atoms. A similar diffusive process could be responsible for the formation of the M_3Te_4 phase and its eventual conversion to Sb_2Te_3. We propose two possible mechanisms based on the motion of atomic steps at or near the δ-Sb_2Te_3 interface. A schematic that describes both of these mechanisms is shown in Fig. 7.

The first proposed mechanism for the transformation of M_3Te_4 to Sb_2Te_3 is one in which metal layers are removed or "evaporated" from a δ–five-layered structure interface, and then added or "condensed" at a δ–seven-layered structure interface. An example of this mechanism is shown in Fig. 7a, where a single double-Te stacking fault layer is either growing or receding and moving to another location. The addition of this single double-Te layer to a precipitate elsewhere in the sample would cause this precipitate to grow. The schematic in Fig. 7c describes how this mechanism could rearrange double-Te layers in an M_3Te_4 structure to an Sb_2Te_3 structure. As metal atoms move toward the seven-layered structure (dotted white lines in Fig. 7c), the double-Te layers there decrease their length, (dotted black lines in Fig. 7c) while metal atoms diffuse away from the five-layered structure and the double-Te layers grow in length there. This would result in the widening of plate-like precipitates of Sb_2Te_3 as a result of the long-range diffusion of metal atoms.

The other proposed mechanism provides a way for isolated double-Te layers to translate one close-packed planar spacing via short-range diffusion processes. An HRTEM micrograph suggesting this mechanism is shown in Fig. 7b, where atomic steps in each of the double-Te layers are seen in a thin M_3Te_4 precipitate (indicated by arrows). The lateral motion of these steps would allow the double-Te layers to move "up" or "down" by one close-packed plane spacing. In this way, it is possible both for an

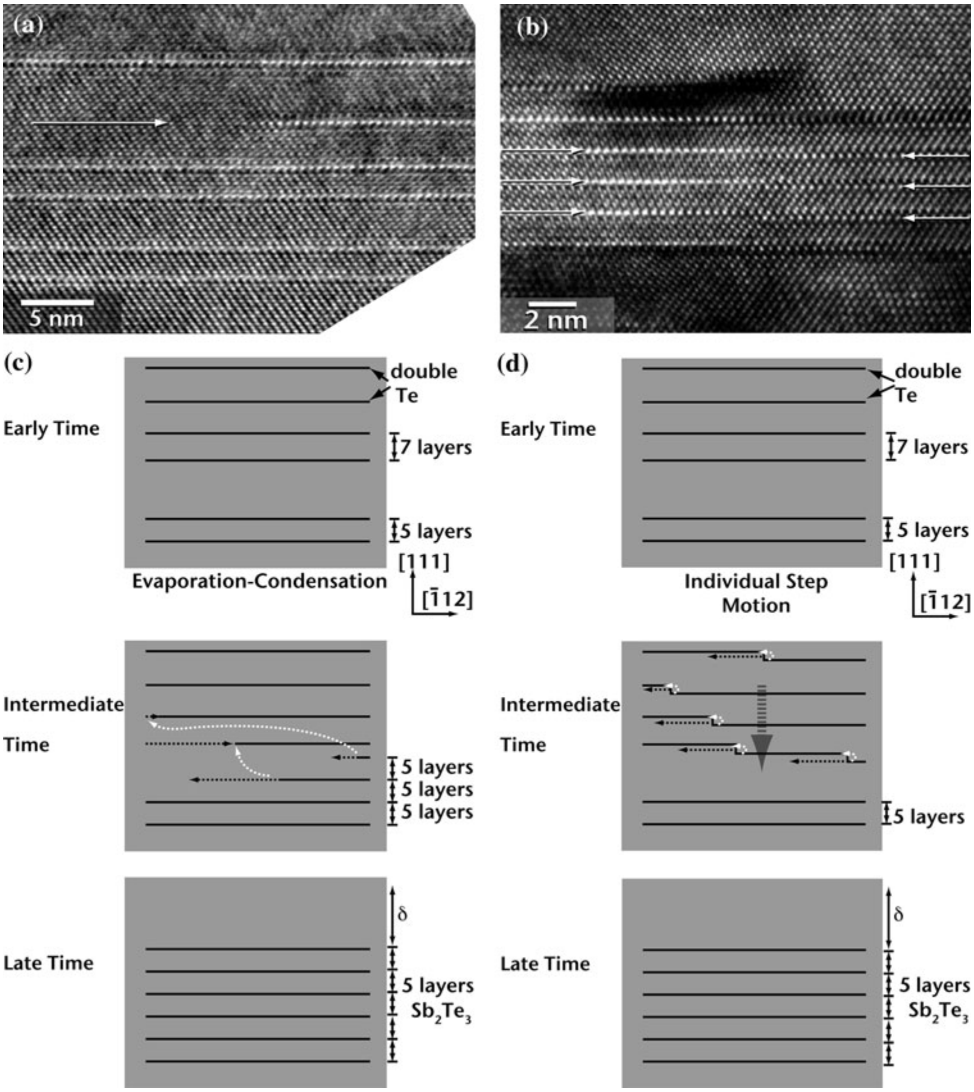

Fig. 7 HRTEM images (**a**), (**b**), and schematics (**c**), (**d**) showing two proposed mechanisms for the transformation of M_3Te_4 to Sb_2Te_3. In the schematics, the black lines represent double-Te layers, *black dotted lines* represent their motion, and *white dotted lines* represent metal flux. For evaporation–condensation, flux of metal causes a double-Te layer to either increase or decrease its length. The example in (**a**) shows an *arrow* that points toward the termination of a double-Te, similar to the terminated double-Te layers at intermediate times in (**c**). For individual step motion, the individual double-Te layers can move one close-packed planar spacing at a time until they are evenly spaced five layers apart. The *arrows* in (**b**) point toward individual steps in the double-Te layers, which is analogous to what is seen at intermediate times in (**d**)

entire M_3Te_4 precipitate to translate by “coordinated step motion” (gray dashed arrow in Fig. 7c), and for a seven-layered structure to convert to a five-layered structure. A schematic of this process is shown in Fig. 7d where individual double-Te layers can translate in directions perpendicular to the close-packed planes. Once the precipitate is adjacent to an Sb_2Te_3 precipitate, the lateral motion of atomic steps can move an individual double-Te layer down one close-packed planar spacing and convert the stacking to a five-layered structure. Again, this mechanism adds double-Te layers to the five-layered structure, and the Sb_2Te_3 precipitates widen.

One kinetic limitation to both these proposed processes is that there must be freely available step nucleation sites for the relocation of double-Te layers. The electron microscopic observations show that at the early stages of the reaction, the stacking faults intersect, and at later stages both the M_3Te_4 and Sb_2Te_3 precipitates intersect and form a typical Widmanstätten structure [39]. These intersecting regions should contain a variety of crystalline defects that can serve as nucleation sites for the formation of new steps. Therefore, the nucleation of new steps should not provide a barrier to advance the transformation process. The slow kinetics of the reaction observed below 350 °C [41] are likely just a result of the process being diffusion limited.

Historically, the literature has shown several disagreeing interpretations of the phase stability in the Ag–Sb–Te system. Since the seven-layered structure is only observed for precipitates tens of nanometers wide, the ability to detect the seven-layered structure is challenging. Previous researchers studying the Ag–Sb–Te system had no prior data that suggested the intermediate phases exist, and since these phases are probably not equilibrium phases, they are even harder to detect at long anneal times. Previous work has shown that a simple eutectoid reaction does not explain the transformations observed at temperatures between 300 and 350 °C [41]. Some of the confusion at low temperature could be due to the fact that intermediate phases are forming, but they were previously undetectable because of their small size and similar interplanar spacings to Sb_2Te_3. Our observation of metastable intermediate phases helps to clarify the phase equilibrium between δ and Sb_2Te_3 on the Sb_2Te_3-rich side of the pseudobinary Ag_2Te–Sb_2Te_3 phase diagram. Specifically, with knowledge of the existence of transition phases, it should be possible to more carefully determine the exact stability limits of the δ phase by accounting for fine-scale metastable phases. We also point out that the presence of nanoscale, metastable second phases and stacking faults, which are difficult to detect without detailed microscopic examination, complicates thermoelectric property measurement of the δ phase. These microstructural features provide parallel conduction paths, which can affect charge carrier and phonon transport [39].

Conclusions

This study focused on the microstructural evolution during the precipitation of Sb_2Te_3 in a rocksalt Ag–Sb–Te phase. The microscopic observations and the bulk X-ray diffraction measurements both confirmed the existence of a metastable seven-layered structure based on the chemical formula M_3Te_4. This intermediate phase provides a route for incremental compositional changes during the precipitation of Sb_2Te_3. Our analysis suggests the following steps in the transformation process:

1. The formation of individual double-Te layers in the δ phase.
2. The agglomeration of these double-Te layers into plates hundreds of nanometers wide with a distribution in the double-Te layer separation peaked at seven close-packed planar spacings.
3. The motion of the double-Te layers by a combination of evaporation–condensation and individual double-Te step motion to produce the five-layered Sb_2Te_3 structure.

More generally, the present results provide insight concerning the mechanisms controlling microstructural evolution in rocksalt/tetradymite-structured chalcogenides. This work should be pertinent to understanding the factors controlling interface formation as well as long-term aging and stability in this broad class of important thermoelectric materials.

Acknowledgements The authors gratefully thank Paul Kotula for help with AXSIA and the MSA/MCR analysis, Miles Clift for EMPA, and the useful suggestions of Norm Bartelt, Jessica Lensch-Falk, and Peter Sharma. Sandia is a multiprogram laboratory operated by Sandia Corporation, a Lockheed Martin Co., for the United States Department of Energy under Contract No. DE-AC04-94-AL85000. Support was provided in part by DOE-OBES-DMS and the Sandia LDRD office.

References

1. Dresselhaus MS, Chen G, Tang MY et al (2007) Adv Mater 19:1043
2. Faleev SV, Léonard F (2008) Phys Rev B Condens Matter Mater Phys 77:214304
3. Medlin DL, Snyder GJ (2009) Curr Opin Colloid Interface Sci 14:226
4. Kanatzidis MG (2010) Chem Mater 22:648
5. Snyder GJ, Toberer ES (2008) Nat Mater 7:105
6. Skrabek EA, Trimmer DS (1995) In: Rowe DM (ed) CRC handbook of thermoelectrics. CRC Press, New York
7. Hsu KF, Loo S, Guo F et al (2004) Science 303:818
8. Marin RM, Brun G, Tedenac JC (1985) J Mater Sci 20:730. doi: 10.1007/BF01026548
9. Sugar JD, Medlin DL (2009) J Alloys Compd 478:75
10. Matsushita H, Hagiwara E, Katsui A (2004) J Mater Sci 39:6299. doi:10.1023/B:JMSC.0000043599.86325.ba
11. Rosi FD, Hockings EF, Lindenblad NE (1961) RCA Rev 22:82
12. Marin RM, Ferdjallah L, Brun G, Tedenac JC (1985) Mater Res Bull 20:107
13. Morelli DT, Jovovic V, Heremans JP (2008) Phys Rev Lett 101:035901
14. Jovovic V, Heremans JP (2009) J Electron Mater 38:1504
15. Irie T (1962) J Phys Soc Jpn 17:1810
16. Armstrong RW, Faust JWJ, Tiller WA (1960) J Appl Phys 31:1954
17. Wolfe R, Wernick JH, Haszko SE (1960) J Appl Phys 31:1959
18. Cook NJ, Ciobanu CL, Wagner T, Stanley CJ (2007) Can Miner 45:665
19. Ikeda T, Collins LA, Ravi VA, Gascoin FS, Haile SM, Snyder GJ (2007) Chem Mater 19:763
20. Ikeda T, Haile SM, Ravi VA, Azizgolshani H, Gascoin F, Snyder GJ (2007) Acta Mater 55:1227
21. Ikeda T, Ravi VA, Collins LA, Haile SM, Snyder GJ (2007) J Electron Mater 36:716
22. Ikeda T, Ravi VA, Snyder GJ (2009) Acta Mater 57:666
23. Frangis N, Kuypers S, Manolikas C, Van Landuyt J, Amelinckx S (1989) Solid State Commun 69:817
24. Frangis N, Kuypers S, Manolikas C, Van Tendeloo G, Van Landuyt J, Amelinckx S (1990) J Solid State Chem 84:314
25. Maier RG (1963) Z Metallkd 54:311
26. Stegherr A, Wald F, Eckerlin P (1961) Z Naturforsch A 16:130
27. Villars P, Prince A, Okamoto H (1995) Handbook of ternary alloy phase diagrams. ASM International, Materials Park, OH
28. Cliff G, Lorimer GW (1975) J Microsc 103:203
29. Williams DB, Carter CB (1996) Transmission electron microscopy: a textbook for materials science. Plenum Press, New York
30. Keenan MR (2009) Surf Interface Anal 41:79
31. Keenan MR, Kotula PG (2003) US Patent 6584413
32. Keenan MR, Kotula PG (2004) US Patent 6675106
33. Keenan MR, Kotula PG (2004) Surf Interface Anal 36:203
34. Kotula PG, Keenan MR, Michael JR (2003) Microsc Miroanal 9:1
35. Parish CM, Brennecka GL, Tuttle BA, Brewer LN (2008) J Am Ceram Soc 91:3690
36. Kotula PG, Keenan MR (2006) Microsc Miroanal 12:538
37. Fiori C, Swyt-Thomas C, Myklebust B. http://www.cstl.nist.gov/div837/Division/outputs/DTSA/oldDTSA.htm
38. Medlin DL, Sugar JD (2010) Scr Mater 62:379
39. Sharma PA, Sugar JD, Medlin DL (2010) J Appl Phys 107:113716
40. Bos JWG, Zandbergen HW, Lee MH, Ong P, Cava RJ (2007) Phys Rev B Condens Matter Mater Phys 75:195203
41. Burmeister RA, Stevenson DA (1964) Trans Metall Soc AIME 230:329